Received: 12 November 2021 | Revised: 9 February 2022 | Accepted: 26 February 2022

DOI: 10.1111/jmi.13096

Journal of Microscopy RMS

ORIGINAL ARTICLE

Individual fibre separation in 3D fibrous materials imaged by X-ray tomography

Dorian Depriester[1,*] | **Sabine Rolland du Roscoat**[1] | **Laurent Orgéas**[1] | **Christian Geindreau**[1] | **Benjamin Levrard**[2] | **Florian Brémond**[2]

[1]3SR, UMR 5521, Université Grenoble Alpes, CNRS, G-INP, Grenoble, France

[2]Michelin Corporation, European Center of Technologies, Clermont-Ferrand, France

Correspondence
Sabine Rolland du Roscoat, University of Grenoble Alpes, CNRS, G-INP, 3SR Lab., UMR 5521, F-38000 Grenoble, France.
Email: sabine.rollandduroscoat@3sr-grenoble.fr

[*]**Present Address** Dorian Depriester, Arts et Metiers Institute of Technology, MSMP, HESAM Université, F-13617 Aix-en-Provence, France

Funding information
Institut Carnot PolyNat, Grant/Award Number: ANR16-CARN-0025; Labex Tec21, Grant/Award Number: ANR-11-LABX-0030

Summary

Modelling the physical behaviour of fibrous materials still remains a great challenge because it requires to evaluate the inner structure of the different phases at the phase scale (fibre or matrix) and the at constituent scale (fibre). X-ray computed tomography (CT) imaging can help to characterize and to model these structures, since it allows separating the phases, based on the grey level of CT scans. However, once the fibrous phase has been isolated, automatically separating the fibres from each other is still very challenging. This work aims at proposing a method which allows separating the fibres and localizing the fibre–fibre contacts for various fibres geometries, that is: straight or woven fibres, with circular or non-circular cross sections, in a way that is independent of the fibres orientations. This method uses the local orientation of the structure formed by the fibrous phase and then introduces the misorientation angle. The threshold of this angle is the only parameter required to separate the fibres. This paper investigates the efficiency of the proposed algorithm in various conditions, for instance by changing the image resolution or the fibre tortuosity on synthetic images. Finally, the proposed algorithm is applied to real images or samples made up of synthetic solid fibres.

KEYWORDS

3D fibrous materials, contact identification, fibre separation, microstructural descriptors, X-ray tomography

Notations

- $\tilde{\alpha}$ Misorientation angle.
- $\bar{\alpha}^{\mathrm{th}}$ Threshold value on $\tilde{\alpha}$.
- $\mathrm{dc}_P(\mathrm{t}^i)$ Half-chord length in P along t^i.
- $\mathscr{D}_{\mathrm{iso}}$ Isotropic dilation operator.
- $\mathscr{D}_{||}$ Dilation operator parallel to $\bar{\mathrm{u}}$.
- $\mathbf{e}_n$ n-th direction associated to the reference frame.
- $\mathbf{F}_k$ Set of voxels belonging to the fibre k.
- $\mathbf{I}_P$ Inertia matrix in $P \in \Omega^{\mathrm{f}}$.
- λ Slenderness ratio.
- n_t Number of investigated values of t^i.
- n_f Number of identified fibres.
- n_{orph} Number of voxels in Ω_{orph}.
- Ω^{f} Fibrous phase.
- $\Omega^{\mathrm{f}}_{\mathrm{mult}}$ Multiple points, resulting from the dilatation operation.
- Ω_{orph} Subset of voxels in Ω^{f} which are not allocated to any fibre.
- P Considered voxel in Ω^{f}.
- ψ Azimuth angle.
- $\bar{r}$ Mean fibre radius.
- θ Elevation angle (latitude).

 © 2022 Royal Microscopical Society

$\mathbf{t}^i$ i-th computation direction for $\mathrm{dc}_P(\mathbf{t}^i)$
$\bar{\mathbf{u}}$ Mean orientation of a single fibre.
$\mathbf{u}_P^{\mathrm{I}}$ Minor axis of the inertia matrix I_P.

subscripts: Voxel index (P) or fibre index (k)
superscripts: Computational direction index (i) or eigenvalue indices (I, II and III)

1 | INTRODUCTION

It is well known that the macroscopic behaviour of fibrous materials is inherited from their microscopic composition and microstructure.[1] Their physical properties depend on the volume fraction of fibres but also on their geometries and 3D spatial repartitions (orientation and fibre–fibre contacts). Their microstructures have been studied for the last 20 years using X-ray microtomography.[2–4] This technique allows imaging the inner structure of materials that are opaque to visible light and gives valuable information about the 3D spatial distribution of each phase. Nevertheless, the analysis of fibre–fibre contacts and the geometrical characterization of the fibres is still challenging because it requires to numerically separate the fibres from computed tomography (CT) images. For soli[5–7] Another method consists in first extracting the centrelines of the fibres, also called skeletonization algorithm.[8] Usually, the skeleton is defined by a series of control points and a piecewise-defined and smooth function (e.g. splines). Once the skeleton is computed, the main branches can be used to define each fibre. The skeletonization can be made manually[9] or automatically.[10,11] In the general case, one would use the 3D euclidean distance map[12,13] or homotopic thinning[14–16] to skeletonize the fibrous phase. However, skeleton-based methods are restricted to low volume fraction and fibres exhibiting nearly isotropic cross sections. For hollowed fibres, such as wood pulp fibres, specific algorithm may be used, usually based on the lumen tracking.[17,18] In more complex fibrous media, other methods are based on the local orientation of the structure. Some authors[19,20] use grey level images for evaluating a structure tensor, computed from the convolution of Gaussian distributions in the vicinity of each considered voxel. Eberhardt and Clarke[21] used the chord lengths whereas Naouar et al.[22] computed the grey level co-occurrence matrix (GLC Matrix).[23] Miletić et al.[24] used the greyscale gradient of the images to track the surface of each fibre. In binarized images, orientation characterization is usually based on the morphologies of the objects. Sandau and Ohser[25] proposed to evaluate the local orientation from the oriented chord lengths. Some authors used the last method to compute either the local inertia matrices[26] or the structure tensor[27]. Miettinen et al.[28] also used the Gaussian convolution to compute the structure tensor from binarized images. In each method resulting in a structure tensor or an inertia matrix, the local orientation can be evaluated by solving the eigenvalue problem. Once the local orientations are characterized, the separation of the fibres is usually made based on the local changes of these orientations. Naouar et al.[22] used the homogeneity parameter[29] to separate warp and weft yarns in CT grey-level images of a 3D textile. Viguié et al.[27] evaluated the local change (called 'mean angular deviation') along the horizontal plane of this axis on binarized images. Thus, it was possible to separate the fibre in CT images by thresholding the mean angular deviation. After separation, the fibres were fully reconstructed using a recursive anisotropic dilation (dilation along the mean fibre direction). This method lead to valuable results on various media but it was still restricted to networks with planar fibre orientations.

It is worth mentioning that recent advances in artificial intelligence (AI) have brought novel techniques for automatic detection of shapes or patterns in 2D or 3D images; still, only few authors[30,31] used convolution neural network to separate fibres in CT images. This is because of the large amount of data required for training the neural network.

In this work, the separation criterion proposed by Viguié et al.[27] was revisited for fully 3D-oriented medium. Then, the dilation procedure used by the last authors was also improved to make it valid for either straight or woven fibres with 3D local orientation. We first introduce the separation criterion, the reconstruction algorithm and some metrics applied to the fibres. In a second task, we investigate the influence of the parameters used for the separation and the reconstruction of the fibres on the resulting geometry. Then, the proposed algorithm is applied to different media in order to evaluate its ability to separate the fibres in different conditions.

2 | METHOD

2.1 | Example of fibrous medium

In this section, the fibrous medium illustrated in Figure 1 is used as an example of the proposed algorithm. It is constituted of copper fibres with a circular cross section (diameter 200 μm $\approx$ 12 vx) and a mean length of about 10 mm, as detailed elsewhere.[13] Consider that CT image as a 3D regular grid of points (voxels), which belong either to the matrix phase or the fibrous phase. Let Ω^{f} be the subset of voxels corresponding to the fibrous phase. The 3D images are stacks of 2D images (slices) where e_1 and e_2 denote the directions associated to each slice, whereas e_3 denotes the stacking direction. Since the proposed approach is independent of the voxel size, all

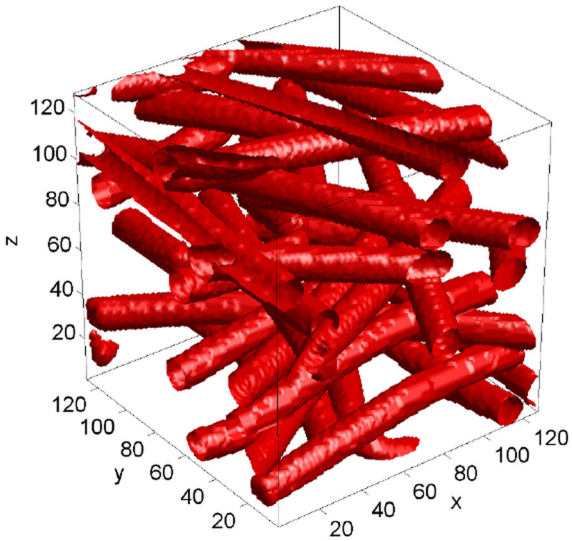

FIGURE 1 Example of a two-phased fibrous material imaged by X-ray tomography: three-dimensional surface rendering of the binarized image. The fibrous phase is represented as a red solid volume whereas the matrix phase is set to transparent. Dimensions are expressed in voxels

dimensions shown in figures are given in voxels throughout this paper.

2.2 | Description of the overall algorithm

Figure 2 represents the method to identify the fibres and the fibre–fibre contacts from a binarized CT image, that is a 3D image where the fibrous phase is already identified. This algorithm is composed of three steps: step ① refers to the separation of fibres, step ② refers to the reconstruction of the fibres and step ③ deals with the analyses of contacts and fibres geometries.

2.3 | Step 1: Fibres Separation

2.3.1 | Computation of the chord lengths

Let $\mathbf{t}^i$ be a given direction and t_1^i, t_2^i and t_3^i its coordinates in the reference frame ($\mathbf{t}^i = t_1^i e_1 + t_2^i e_2 + t_3^i e_3$). Consider a voxel $P \in \Omega^{\mathrm{f}}$; the distance from P to the matrix along $\mathbf{t}^i$, denoted $d_P(\mathbf{t}^i)$ below, is computed using the method proposed by Altendorf and Jeulin.[26] Appendix A provides some details about this method. These distances can be used to compute the half-chord length in P, denoted $\mathrm{d}c_P(\mathrm{t}^i)$, as defined by Sandau and Ohser[25]:

$$\forall i = 1, \dots, n_t \quad \mathrm{d}c_P(\mathrm{t}^i) = \frac{d_P(\mathbf{t}^i) + d_P(-\mathbf{t}^i)}{2}, \tag{1}$$

where n_t denotes the number of investigated directions $\mathbf{t}^i$.

2.3.2 | Local orientation

In $P \in \Omega^{\mathrm{f}}$, Altendorf and Jeulin[26] define the inertia matrix $\mathbf{I}_P$ such that:

$$\mathbf{I}_P = \frac{1}{n_t} \sum_{i=1}^{n_t} \left(\mathrm{d}c_P(\mathrm{t}^i)\right)^2 \boldsymbol{M}(\mathbf{t}^i) \tag{2}$$

with:

$$\boldsymbol{M}(\mathbf{t}^i) = \frac{1}{\|\mathbf{t}^i\|^2} \begin{bmatrix} {t_2^i}^2 + {t_3^i}^2 & -t_1^i t_2^i & -t_1^i t_3^i \\ -t_1^i t_2^i & {t_1^i}^2 + {t_3^i}^2 & -t_2^i t_3^i \\ -t_1^i t_3^i & -t_2^i t_3^i & {t_1^i}^2 + {t_2^i}^2 \end{bmatrix}, \tag{3}$$

where $\|\mathbf{t}^i\|$ denotes the euclidean norm of $\mathbf{t}^i$.

Let $I_P^{\mathrm{I}} \leq I_P^{\mathrm{II}} \leq I_P^{\mathrm{III}}$ be the eigenvalues of $\mathbf{I}_P$ and $\mathbf{u}_P^{\mathrm{I}}$, $\mathbf{u}_P^{\mathrm{II}}$, $\mathbf{u}_P^{\mathrm{II}}$ the corresponding normalized eigenvectors. For a given fibre, its orientation is characterized by its lowest inertia momentum. In other words, the minor axis of $\mathbf{I}_P$ (denoted $\mathbf{u}_P^{\mathrm{I}}$ above) gives the local orientation of the fibrous phase in P. Figure 2B illustrates the local orientations $\mathbf{u}_P^{\mathrm{I}}$ (white arrows) computed in the medium introduced in Figure 1. It is clear that, away from the contact zones, local orientations appear to be fairly aligned with the macroscopic orientation of each fibre. On the contrary, contact zones (e.g. with coordinates around (35,95) in Figure 2D) are characterized by large changes in the local orientations.

2.3.3 | Misorientation angle

For a given voxel $P \in \Omega^{\mathrm{f}}$, let N_P be the subset of voxels in Ω^{f} and in contact with P, considering its 26-connected neighbourhood. Let $\tilde{\alpha}$ be the misorientation angle, expressed in radian-per-voxel, so that:

$$\tilde{\alpha}_P = \frac{1}{\tilde{\delta}} \sum_{Q \in \mathrm{N}_P} \frac{\angle\left(\mathbf{u}_P^{\mathrm{I}}, \mathbf{u}_Q^{\mathrm{I}}\right)}{\|\mathbf{PQ}\|} \quad \text{with} : \tilde{\delta} = \sum_{P \in \mathrm{N}_P} \frac{1}{\|\mathbf{PQ}\|}, \tag{4}$$

where $\angle(\mathbf{u}_P^{\mathrm{I}}, \mathbf{u}_Q^{\mathrm{I}})$ denotes the bearing angle between $\mathbf{u}_P^{\mathrm{I}}$ and $\mathbf{u}_Q^{\mathrm{I}}$. This definition of the misorientation angle is a 3D generalization of the mean angular deviation introduced by Viguié et al.[27] Here, the angular values are weighted by the inverse of the distance from the central point. Figure 2B illustrates the misorientation map (colourmap), evidencing the previous observations (e.g. coordinates around (35,95)). In the investigated media, this misorientation angle is typically larger than 5° near contacts. On the

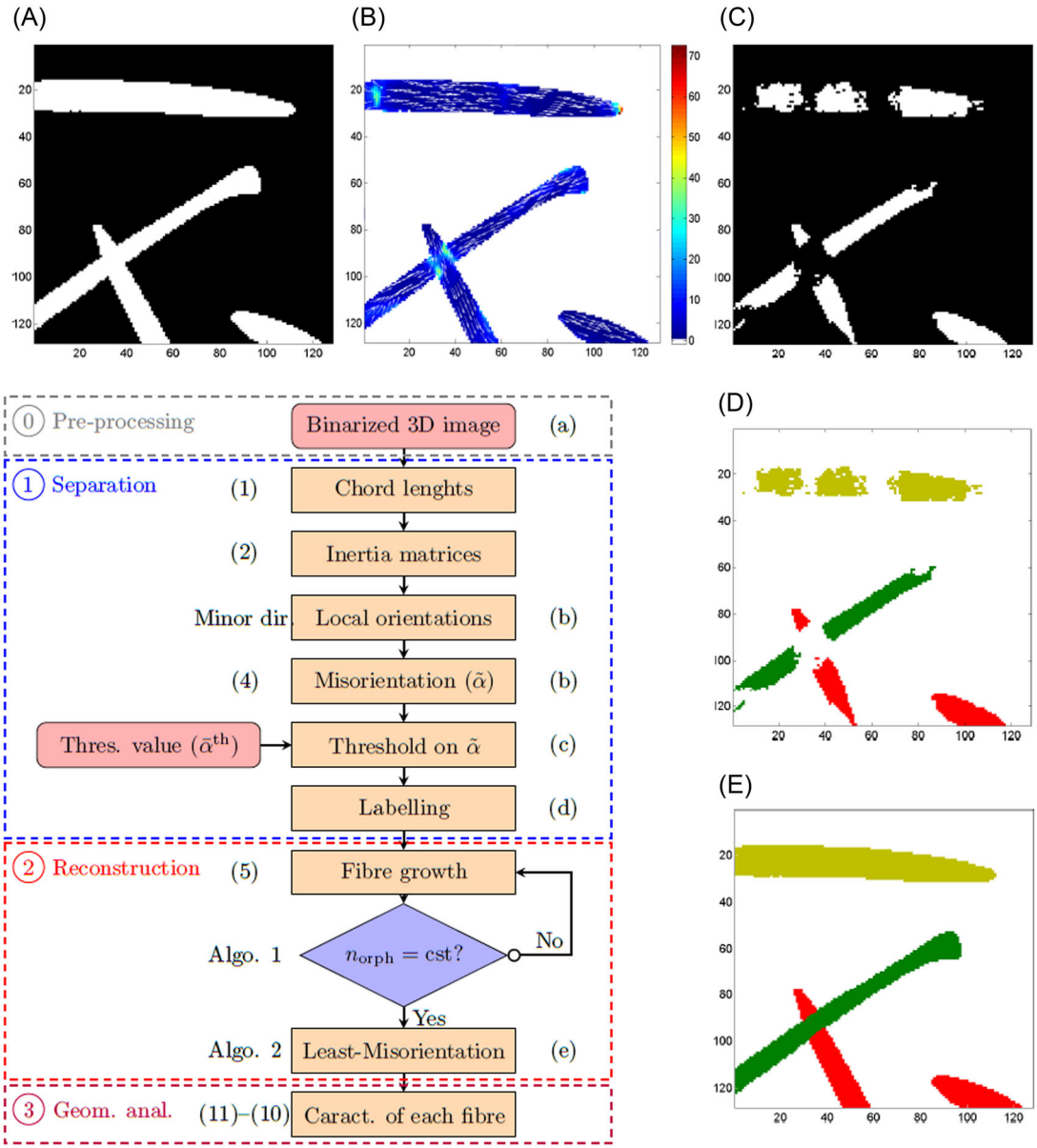

FIGURE 2 Scheme of the overall proposed algorithm to separate the fibres, reconstruct them, track the fibre–fibre contacts and characterize the fibre geometries. The first block (which aims to separate the fibrous phase from the matrix phase) is not detailed in this work. Despite the fact that all the steps are computed in 3D, the intermediate steps are illustrated in this figure as 2D slices (at $z = 80$) taken from the example medium (see Figure 1): (A) threshold on the grey level image, (B) misorientation angle, (C) threshold on the misorientation and results from (D) labelling then (E) reconstruction

opposite, the misorientation angle is close to 0° away from the contact zones.

2.3.4 | Thresholding and labelling

Based on the previous considerations, one can separate fibres in contact using a threshold value $\bar{\alpha}^{th}$ on $\tilde{\alpha}$, as illustrated in Figure 2C. Once the fibres are separated, each one can be considered as a set of voxels, defined as a 3D connected region. Therefore, the fibres can be labelled using a standard flood-fill algorithm,[32] associating a unique integer to each connected region, as illustrated in Figure 2D. In this paper, F_k and n_f denote the subset of voxels which belong to the fibre labelled k and the number of identified fibres, respectively. When thresholding $\tilde{\alpha}$, some very small disconnected regions may arise. In order to remove these unrealistic outliers from the labelled regions, regions smaller than a given number of voxels were discarded. The number of discarded regions and their associated volumes mainly depend on the image resolution and the number of contacts.

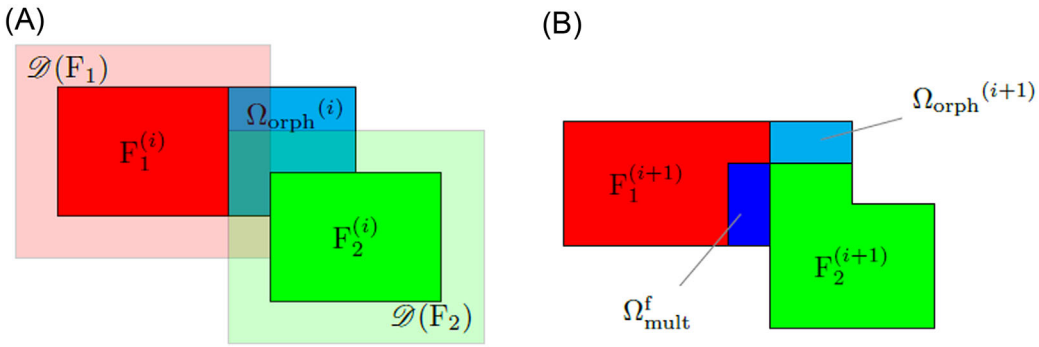

FIGURE 3 Schematic representation of the Boolean operations used for dilation: two fibres are represented (F_1 and F_2); the dilation is restricted to Ω_{orph}, as defined in (5). (A) At the i-th dilation step and (B) results at the next one. The set Ω^f_{mult} represents the points that belong to both the dilated objects (introduced in Section 2.4.2)

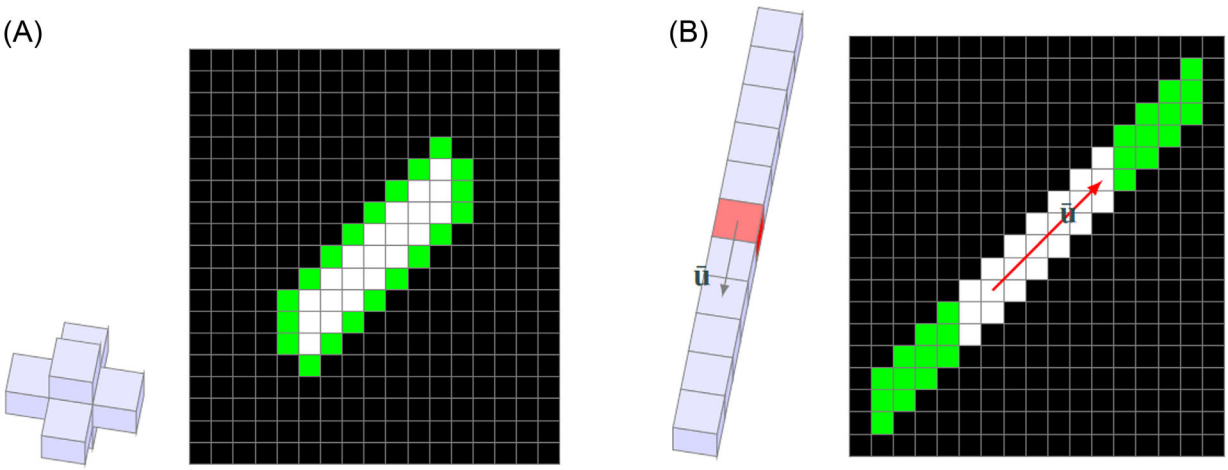

FIGURE 4 Schematic representation of applying either (A) isotropic or (B) longitudinal dilations on a set of voxels (represented in white). The result from dilation is represented in green. In each case, the structuring element[33] is represented (left-hand side)

2.4 | Step 2: Fibre reconstruction

As illustrated in Figure 2D, at this stage of the algorithm, about 30% of the voxels belonging to the fibrous phase are not affected to a labelled fibre. Let Ω_{orph} be this set, consisting in n_{orph} orphan voxels. To allocate these voxels to a fibre, recursive dilations[27] on each identified fibre k are applied:

$$F_k^{(i+1)} = F_k^{(i)} \cup \left(\mathscr{D}\left(F_k^{(i)}\right) \cap \Omega_{orph}{}^{(i)}\right), \tag{5}$$

where i is the iteration step and $\mathscr{D}$ is the dilation operator, described hereafter. Figure 3 illustrates the previous equation as a Venn diagram. This operation is iterated until Ω_{orph} is stabilized. Algorithm 1 gives the pseudo-code associated to this procedure. A dilation operation is defined for a given kernel. The two types of kernels used in this paper, illustrated in Figure 4, are described below.

Algorithm 1 Iterative fibre growth: this operation is performed until the number of elements in Ω_{orph} (n_{orph}) converges.

$\Omega_{orph} \leftarrow$ orphan voxels
$n_{orph} \leftarrow \text{card}(\Omega_{orph})$
while $n_{orph} \neq$ constant **do**
  for all $k = 1$ **to** n_f **do**
    dilation of F_k (eq. 5)
  end for
  $\Omega_{orph} \leftarrow$ orphan voxels
  $n_{orph} \leftarrow \text{card}(\Omega_{orph})$
end while

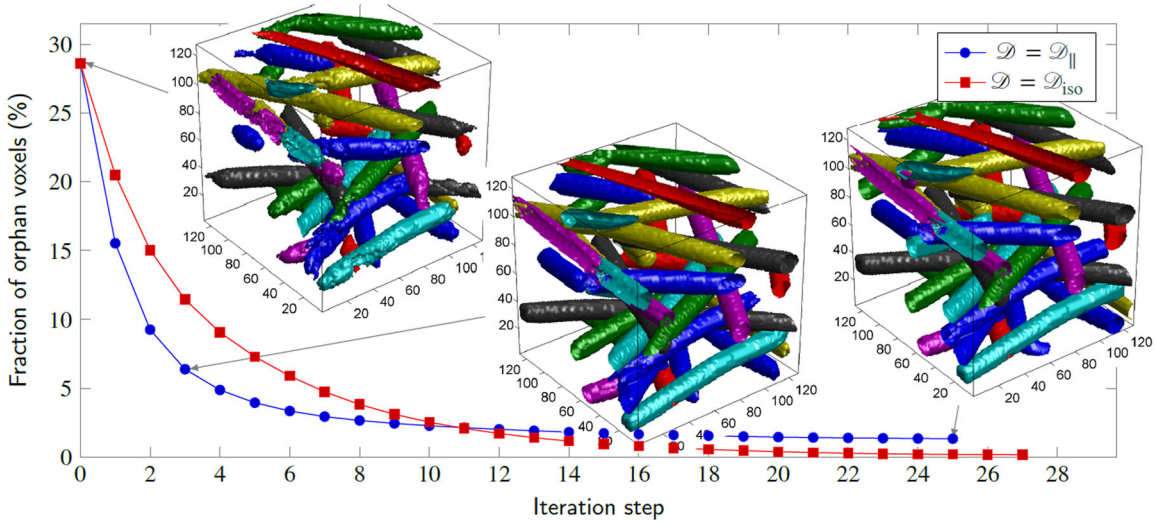

FIGURE 5 Evolution of the fraction of orphan voxels among all the fibrous phase, as a function of the iteration step, when applying longitudinal or isotropic dilations

2.4.1 | Isotropic and longitudinal dilations

The first kernel is an isotropic kernel constituted of 6-connected neighbourhood. The effect of using the isotropic kernel for dilation is schematically illustrated in Figure 4A.

The structuring element with planar orientation used by Viguié et al.[27] was improved to make it suitable for full 3D orientations. Thanks to the mean orientation $\bar{u}$ of each identified fibre (see Section 2.5.1 for details), one can construct a structuring element parallel to $\bar{u}$. The longitudinal dilation operator, denoted $\mathcal{D}_{||}(F_k)$, aims at dilating the fibre F_k along its mean direction $\bar{u}_k$. The effect of using the longitudinal dilation is schematically illustrated in Figure 4B. For a considered voxel, the structuring element used for the longitudinal dilation is composed of a series of elements parallel to $\bar{u}$, as illustrated in Figure 4B. In this work, the range used for the longitudinal dilation was 5 vx (as shown in the last figure) in order to reduce the aliasing effects.

The evolution of the fraction of orphan voxels at each iteration step is plotted in Figure 5, for each dilation operator. It appears that the early iteration steps of the isotropic dilation are slower than the ones of longitudinal dilations, mainly because of the size of structuring elements used for the dilations. On the contrary, at the end of the process, the longitudinal dilation leaves some orphan voxels whereas n_{orph} converges towards 0 when using the isotropic dilations. The differences between the two kinds of dilation are discussed in Section 3.2. Figure 5 also illustrates the results from longitudinal dilation after separation on the example medium (introduced in Figure 1) in terms of geometry. According to this figure, it is clear that the procedure quickly converges towards the final geometry as n_{orph} converges towards its final value.

2.4.2 | Multiple points

When recursively applying the dilation operation, some points may be allocated to several fibres at once, as schematically represented in Figure 3 and depicted in Figure 6. Let Ω^{f}_{mult} be this set of multiple points, as defined

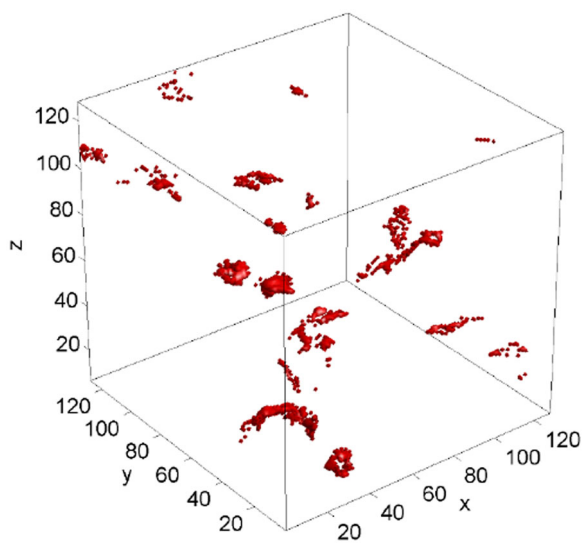

FIGURE 6 Multiple points resulting from the recursive dilations on copper fibres (1471 points)

below:

$$\Omega^{\mathrm{f}}_{\mathrm{mult}} = \bigcup_{k=1}^{n_{\mathrm{f}}} \left(\bigcup_{k'=k+1}^{n_{\mathrm{f}}} (\mathrm{F}_k \cap \mathrm{F}_{k'}) \right). \tag{6}$$

The proposed method to allocate these multiple points in a deterministic manner is the 'least-misorientations method'. To ascribe these voxels to a single fibre, the principle is first to temporary allocate the multiple points to one fibre, then to recompute the local orientations and the misorientations (as defined in Section 2.3.2) in the considered fibre. The same is done with all candidate fibres, allowing to evaluate its resulting misorientations for each fibre. Finally, this voxel is allocated to the fibre leading to its least misorientation. In other words, multiple points are allocated to the fibres in a way that maximizes the straightness of each fibre. This procedure is summed up in Algorithm 2.

Algorithm 2 Least-misorientation method. $A_{P,k}$ denotes the tabular data, containing the misorientation value in P assuming that $P \in \mathrm{F}_k$.

for all $k = 1$ **to** n_{f} **do**
  $\mathrm{F}_{\mathrm{tmp}} \leftarrow \mathrm{F}_k \cup \Omega^{\mathrm{f}}_{\mathrm{mult}}$ // *Consider that* $\Omega^{\mathrm{f}}_{\mathrm{mult}}$ *belongs to* F_k
  Compute $\tilde{\alpha}$, considering only $\mathrm{F}_{\mathrm{tmp}}$
  for all $P \in \Omega^{\mathrm{f}}_{\mathrm{mult}}$ **do**
    $A_{P,k} \leftarrow \tilde{\alpha}_P$ // *Store the resulting misorientation at P*
  end for
end for
for all $P \in \Omega^{\mathrm{f}}_{\mathrm{mult}}$ **do**
  $K \leftarrow \arg\min_k(A_{P,k})$ // $P \in \mathrm{F}_K$ *minimizes the misorientation*
  $\mathrm{F}_K \leftarrow \mathrm{F}_K \cup \{P\}$ // *Add P to Fibre K*
end for

2.5 | Step 3: Geometrical analyses

2.5.1 | Mean orientation of a fibre

The method proposed by Woodcock and Naylor[34] was used to evaluate the mean orientation of each fibre. Let $\mathbf{A}_k$ be the mean fabric tensor of fibre F_k, so that:

$$\mathbf{A}_k = \frac{1}{n_k} \sum_{P \in \mathrm{F}_k} \mathbf{u}^{\mathrm{I}}_P \otimes \mathbf{u}^{\mathrm{I}}_P, \tag{7}$$

where n_k is the number of voxels in F_k and $\otimes$ denotes the tensorial product. The largest eigenvalue of $\mathbf{A}_k$ is an estimate of the distribution variance (comprised between $^1/_3$ and 1) and its associated eigenvector, denoted $\bar{\mathrm{u}}_k$ below, is an estimate of the mean orientation of F_k.[19]

2.5.2 | Mean radius

Consider a voxel $P \in \Omega^{\mathrm{f}}$ and its parent fibre F_k with mean orientation $\bar{\mathrm{u}}_k$. For slightly woven fibres, Altendorf and Jeulin[26] give the following equation to evaluate the local radius of the fibre F_k in P, given by the half-chord length measured along $\mathbf{t}^i$:

$$\forall P \in \mathrm{F}_k, \quad r_P(\mathbf{t}^i) = \mathrm{d}c_P(\mathrm{t}^i) \sin \varphi^i_k \tag{8}$$

with $\varphi^i_k = \angle(\bar{\mathrm{u}}_k, \mathbf{t}^i)$. The more parallel $\mathbf{t}^i$ and $\bar{\mathrm{u}}_k$ are, the less the evaluation of $r_P(\mathbf{t}^i)$ is relevant. Hence, the evaluation of the mean radius was made by weighting the local radii based on the sine of φ^i_k:

$$\forall P \in \mathrm{F}_k, \quad \tilde{r}_P = \frac{1}{\sum_i \sin \varphi^i_k} \sum_{i=1}^{n_t} r_P(\mathbf{t}^i) \sin \varphi^i_k. \tag{9}$$

Let $\bar{r}_k$ be the mean radius of F_k. It comes:

$$\bar{r}_k = \frac{1}{n_k} \sum_{P \in \mathrm{F}_k} \tilde{r}_P. \tag{10}$$

2.5.3 | Contact identification

Let F_i and F_j be the volumes associated to two distinct fibres i and j. The set of voxels which belong to the fibre i and are in contact with the fibre j can be defined as follows:

$$\mathrm{C}_{i,j} = \mathrm{F}_i \cap \mathcal{D}_{\mathrm{iso}}(\mathrm{F}_j). \tag{11}$$

3 | CHOICE OF THE PARAMETERS OF THE ALGORITHM

The objective of this section is to propose guidelines to use the algorithm summarized in Section 2 and to gauge the errors made on the identification of the fibres in terms of geometry (length and diameter) and location (position and orientation). For that purpose, the following methodology is applied: (i) a synthetic medium, representative of one of the various fibre networks mentioned in the introduction, is generated, (ii) the influence of one parameter on the fibre identification is gauged and (iii) guidelines are provided.

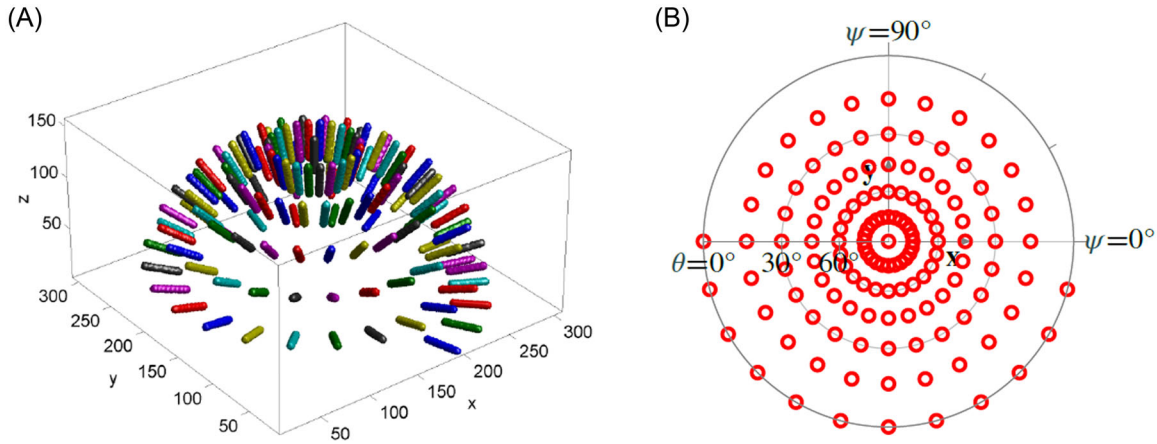

FIGURE 7 Numerically generated medium: (A) 3D view of the hedgehog-like fibrous phase and (B) pole figure of the mean orientation of each fibre (stereographic projection)

3.1 | Computational directions

3.1.1 | Example medium

In order to investigate the effect of increasing the number of computational directions of the chord length (denoted n_t in this paper) on the computation of the mean orientation, a 'hedgehog-like' fibrous medium was numerically generated, as depicted in Figure 7A. In order to avoid the influence of contacts on the evaluation of local orientations, each fibre of this hedgehog was not in contact to each other. These fibres have a nominal length of 35 voxels and two nominal radii are investigated, respectively, 3 and 5 voxels. Fibres were generated for several different orientations, resulting in 133 individual fibres, as illustrated in Figure 7B.

According to Altendorf and Jeulin,[26] the computed directions ($\mathbf{u}_P^{\mathrm{I}}$) undergo an attraction towards each direction $\mathbf{t}^i$. As a result, the set of investigated directions must be balanced so that it leads to an isotropic bias. In other words, the sum of the local inertia matrices, as defined in (3), must be proportional to the identity matrix. Different sets of computed directions were used for evaluating the chord lengths in the hedgehog, resulting in n_t ranging from 13 to 61. These sets are schematically presented in Appendix B (see Figure B1).

3.1.2 | Mean orientations

The mean orientation of each fibre of the hedgehog was evaluated according to the procedure detailed in Section 2.5.1 with different values of n_t. Then, the calculated mean orientations were compared to the theoretical ones, as summed up in Figure 8. In this figure, (ψ, θ) denotes the spherical coordinates (ψ stands for the azimuth angle from e_1, whereas θ denotes the elevation angles towards e_3). In each case, the orientation of fibres lying along the frame directions appears to be accurately evaluated. Since these directions are parallel to the reference frame (see Figure B1), this is in agreement with the theory introduced by Altendorf and Jeulin.[26] On the contrary, the other directions appear to lead to wrong estimates, specially with $n_t = 13$. With $n_t = 25$, all directions characterized by $\theta = 30°$ or $60°$ appear to be well predicted but that with $\theta = 15°, 45°$ and $75°$ lead to largest errors. $n_t = 37$ gives better results for the later orientations without worsening the evaluation of other orientations. When $n_t = 49$ and 61, it is clear that all orientations (except the ones lying along the frame directions) are not accurately evaluated. For the special case $\theta = 0°$, some orientations appear to be 180° off the theoretical ones; this is due to round-off errors and the ambiguous azimuth angle for a horizontal fibre ($(\psi, \theta = 0) \equiv (\psi + \pi, \theta = 0)$ for non-signed orientations).

Figure 9A represents the mean and the largest angular errors between the computed orientations and the theoretical ones for each value of n_t. This plot confirms that the evaluation of the orientations of the hedgehog's fibres is better with $n_t = 37$ than with $n_t = 49$ and 61. The same procedure was used on another 'hedgehog-like' medium with a nominal radius of 5 vx, evidencing the same trend, as illustrated in Figure 9A (red bars). Since the computation of the inertia matrices runs in linear time with n_t, using $n_t = 37$ appears to be the best compromise between execution time and precision. Preliminary tests, not described in this paper, were carried out with hedgehog of various steps. As a result, $n_t = 37$ appears to produce the lowest error regardless the spacing of the hedgehog; thus, all analyses detailed below were done using this value.

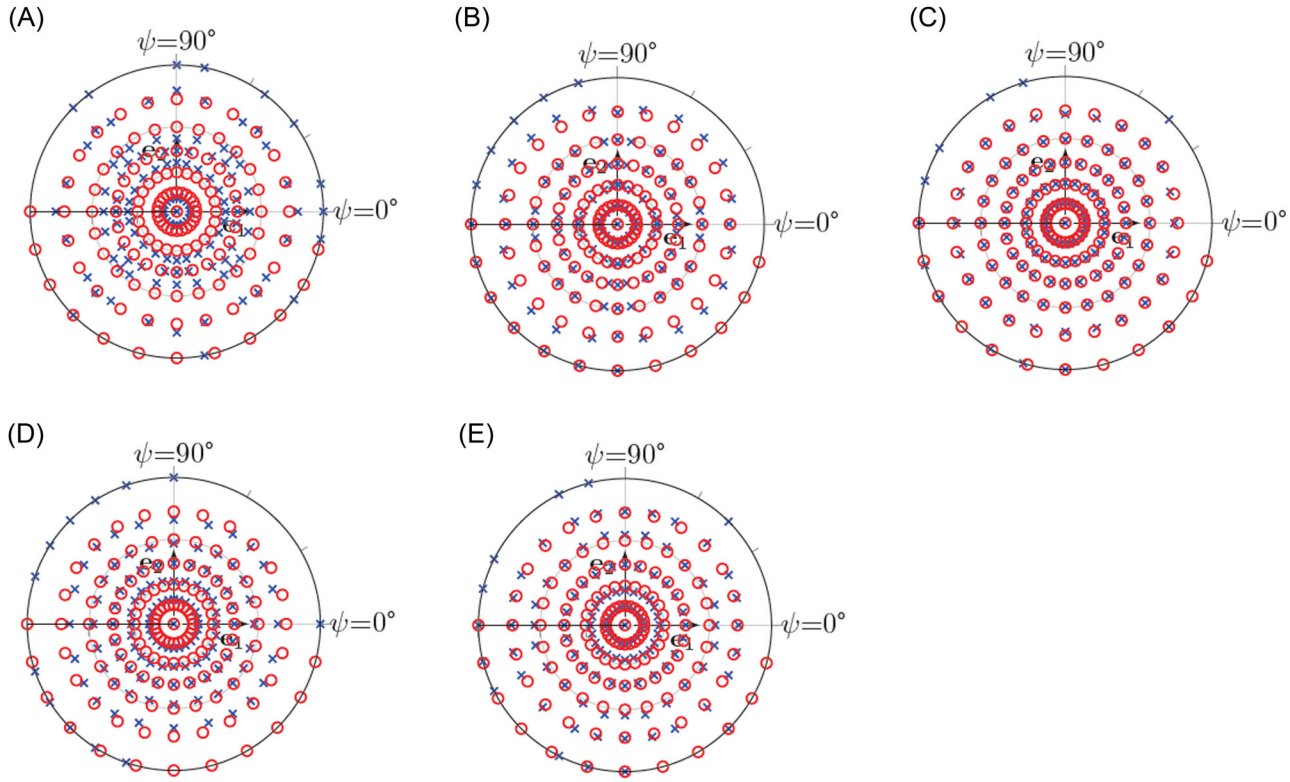

FIGURE 8 Pole figure of the mean orientations of each fibre of the hedgehog (Figure 7), illustrating the influence of the number of computational directions of the chord lengths: (A) $n_t = 13$, (B) $n_t = 25$, (C) $n_t = 37$, (D) $n_t = 49$ and (E) $n_t = 61$. Blue crosses (x) represent the computed orientations whereas the red circles (o) give the theoretical ones, as a comparison. For the sake of readability, the θ axis is not shown (see Figure 7B for details)

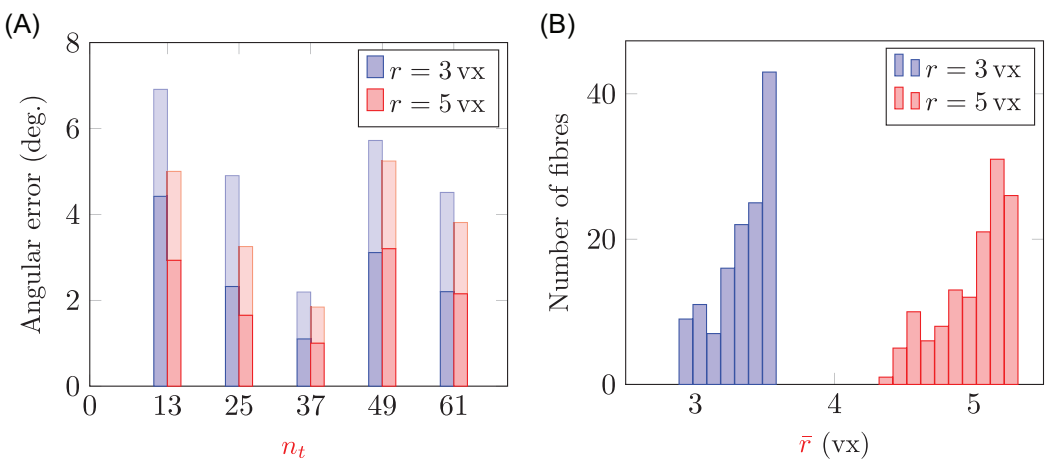

FIGURE 9 Results from the geometrical analyses on the hedgehog: (A) evolution of the mean angular error (darker bars) as a function of n_t, depending on the nominal fibre radius (r), lighter bars give the largest angular error; (B) distribution of the fibres' radii evaluated on the hedgehog (with $n_t = 37$), depending on the nominal radius

3.1.3 | Mean radii

Since the orientation of each fibre is well computed, the evaluation of the mean radius (detailed in Section 2.5.2) can be done. With $n_t = 37$, the computation of the mean radii of the two aforementioned hedgehogs lead to the distributions given in Figure 9B. For the fibres with a nominal radius of 3 vx, the mean value of $\bar{r}$ was 3.41 vx (standard deviation: 0.19); for the fibres with a nominal radius of 5 vx, the mean value of $\bar{r}$ was 4.94 vx (standard

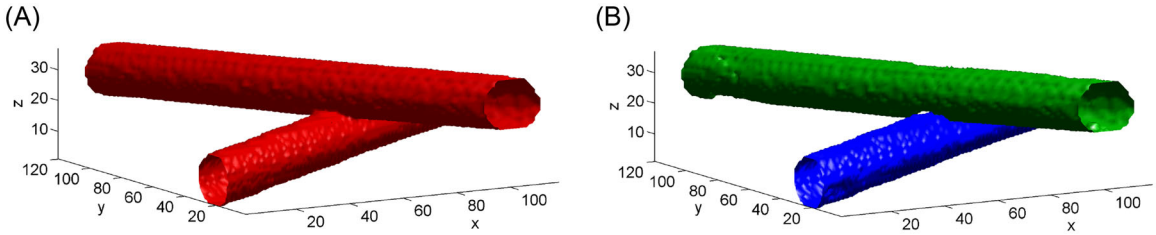

FIGURE 10 Two straight cylindrical fibres (copper). (A) Fibrous phase and (B) separated fibres ($\bar{\alpha}^{\text{th}} = 15°$) before dilation.

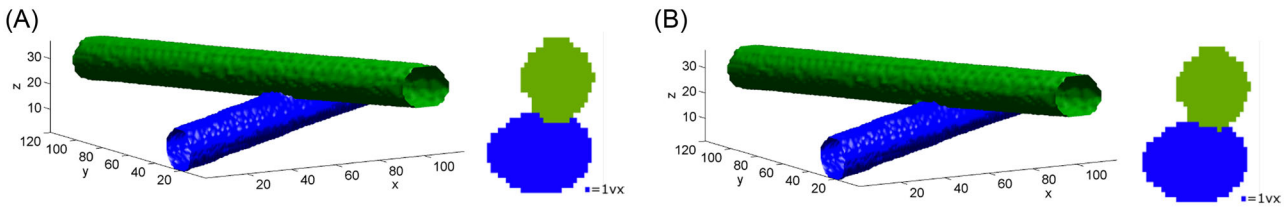

FIGURE 11 Results after (A) isotropic and (B) longitudinal dilations of the fibres presented in Figure 10. Details of the resulting cross sections are given by the 2D sections (at $x = 63$)

deviation: 0.24). Therefore, it appears that the radii are well computed in both cases, leading to slight overestimation for smaller value.

3.2 | Structuring element

3.2.1 | Fibrous networks made up of straight fibres

In order to investigate the influence of the structuring element for the dilation algorithm (i.e. $\mathcal{D} = \mathcal{D}_{\text{iso}}$ vs. $\mathcal{D} = \mathcal{D}_{||}$ in (5)) on the resulting geometries, we considered a medium, characterized by two straight fibres with circular cross section, as illustrated in Figure 10A. These fibres were separated using the separation procedure proposed in this paper, as illustrated in Figure 10B.

After separation of the fibres (Figure 10B), they appear to be well defined, except near the contact zone. As a result, fibres obtained using isotropic dilation are really similar to the ones obtained using longitudinal dilation, as illustrated in Figure 11. Details of the 2D sections illustrate the differences in terms of cross section of each fibre. The isotropic dilation leads to the penetration of the green fibre into the blue one.

3.2.2 | Fibrous networks made up of woven fibres

Now let us consider three wavy fibres, with circular cross section, as illustrated in Figure 12A. They were separated according to the same procedure, leading to the results presented in Figure 12B. The results obtained using isotropic and longitudinal dilation are illustrated in Figures 12C and 12D, respectively. Thus, the differences are evidenced by the remaining orphan voxels (see shaded regions), even after the recursive dilations, when using the longitudinal dilation. Figure 12D shows that the dilation of the green fibre results in a flattened fibre.

3.2.3 | Synthesis

As a conclusion, the following statements can be made:

- longitudinal dilation is recommended for straight fibres because it retains the fibre morphology and leads to better evaluation of the contacts (avoids penetration);
- isotropic dilation is recommended for wavy fibres because it does not leave orphan voxels and does not flatten the fibres.

3.3 | Influence of the geometry

In order to assess the robustness of the proposed algorithm against image quality and morphological parameters, two fibres with cylindrical geometry (with radius $\bar{r} = 10$ vx), in contact to each other, were generated with varying nominal angle (denoted β below) between their axes. In addition, these geometries were generated for different values of the slenderness ratio λ (ratio of length to the diameter). Then, all these geometries were downsampled by a

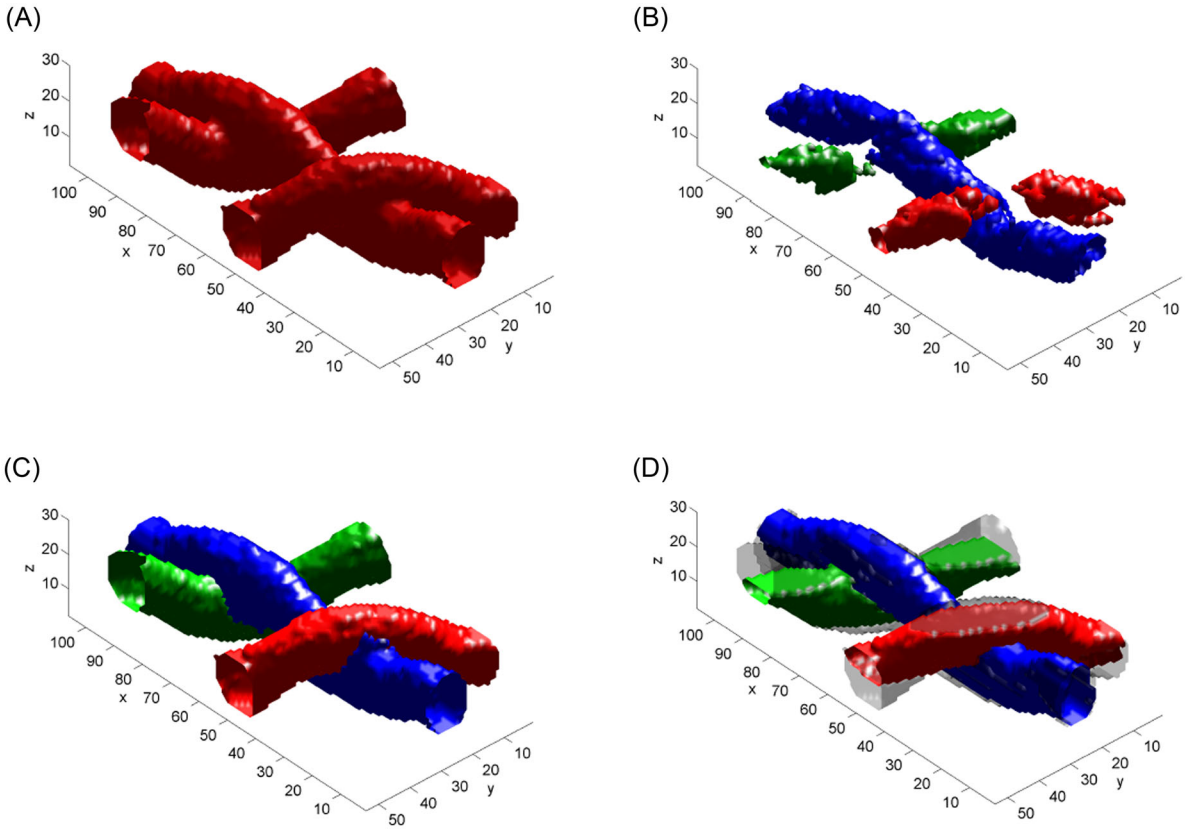

FIGURE 12 Woven cylindrical fibres: (A) binarized fibrous phase, (B) result from separation with $\bar{\alpha}^{\text{th}} = 4°$ and reconstruction using (C) isotropic or (D) longitudinal dilations. Shaded regions correspond to the remaining orphan voxels at the end of the recursive dilation procedure

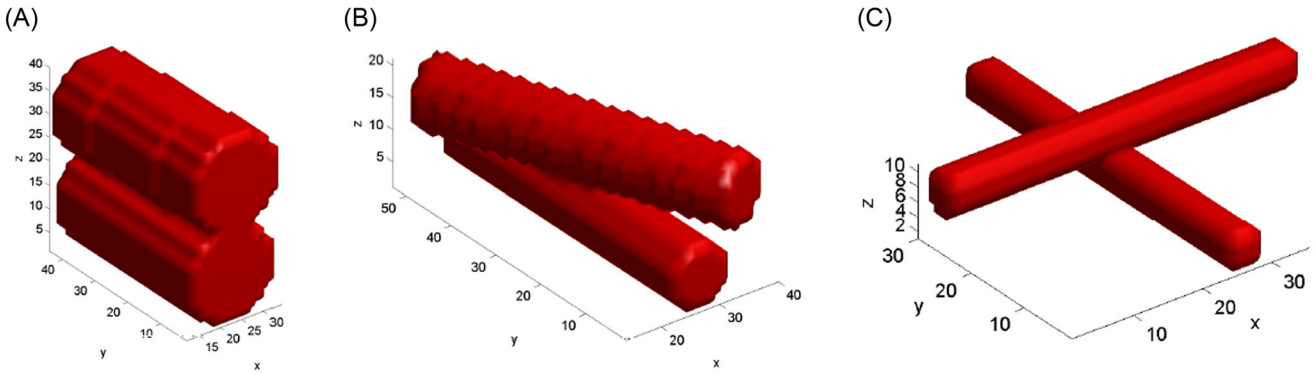

FIGURE 13 Examples of the generated geometries for the investigation of the influence of the image parameters on the separation: (A) $\beta = 3°$, $\lambda = 2$, not downsampled; (B) $\beta = 20°$, $\lambda = 5$, $s = 2$ and (C) $\beta = 90°$, $\lambda = 10$, $s = 4$

factor 2, 3 and 4. In the present section, s denotes the downsampling factor ($s = 1$ corresponds to no downsampling and $s = n$ corresponds to retaining each n-th voxel on each direction). Among all these sets, three geometries are illustrated in Figure 13. Table 1 gives the resulting geometrical parameters (length and diameter) in each case. On each geometry, attempts were made to separate the two fibres using the method detailed in Section 2.3. In each case, the largest thresholding value $\bar{\alpha}^{\text{th}}$ leading to separation of the fibres was recorded, as plotted in Figure 14.

For $\lambda \geq 3$, $\bar{\alpha}^{\text{th}}$ appears to be an increasing function of the angle between the fibres. On the opposite, $\bar{\alpha}^{\text{th}}$ appears to randomly depend on β when $\lambda = 2$. This result indicates that the separation process somehow behaves randomly

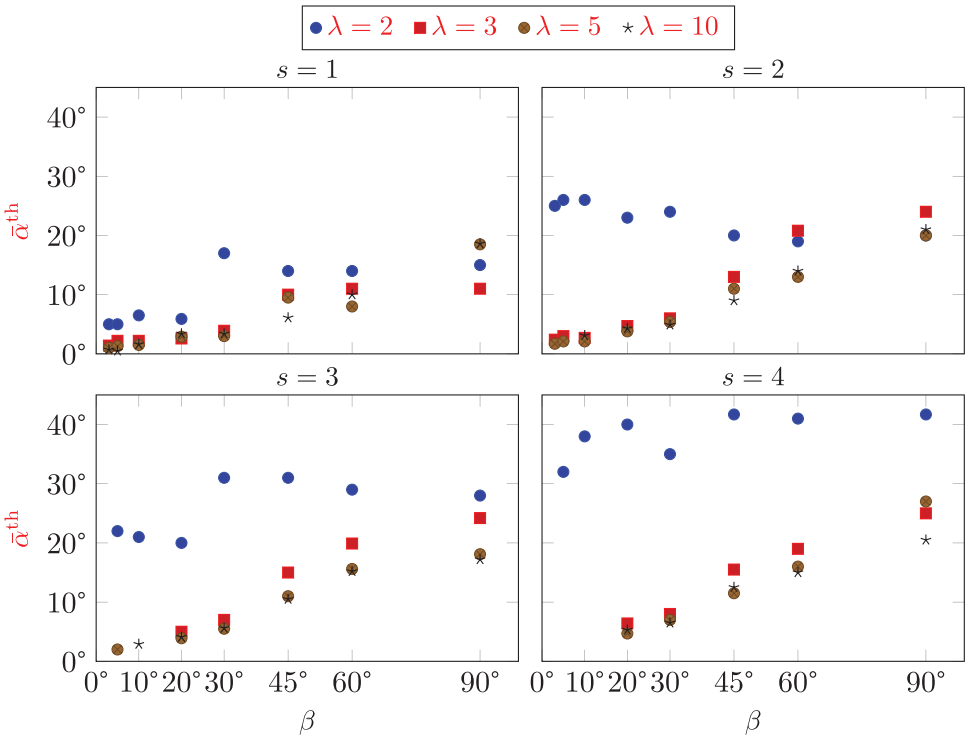

FIGURE 14 Largest values of $\bar{\alpha}^{\text{th}}$ leading to the separation of the generated fibres, as a function of the angle between the two fibres β, the slenderness ratio λ and the downsampling factor s

TABLE 1 Geometrical parameters (radius $\bar{r}$ and length ℓ, in voxels) of the generated fibres, depending on the downsampling factor s and the slenderness ratio λ

		Downsampling factor			
λ		1	2	3	4
2	$\bar{r}$:	10	5	3	2.5
	ℓ:	40	20	12	10
3	$\bar{r}$:	10	5	3	2.5
	ℓ:	60	30	18	15
5	$\bar{r}$:	10	5	3	2.5
	ℓ:	100	50	30	25
10	$\bar{r}$:	10	5	3	2.5
	ℓ:	200	100	60	50

when one attempts to separate short fibres. As a conclusion, the present algorithm seems to work on fibres characterized by $\lambda \geq 3$.

On higher downsampling factor ($s = 4$), the separation process cannot be performed with $\beta < 20°$, whatever the slenderness ratio is. According to the geometrical parameters given in Table 1, it appears that a radius larger than 2.5 vx is required to ensure the ability of the present algorithm to separate the fibres.

As the proposed algorithm is based on the local change in fibre orientation, the separation of fibres nearly parallel to each other ($\beta \sim 0°$) is not possible with the proposed algorithm. In this case, one should use other methods based on skeletonization.[8–11]

3.4 | Wavy fibres: Influence of the wrap angle

In order to investigate the ability of the algorithm to separate wavy fibres wrapped around each other, theoretical geometries were numerically generated, as presented in Figure 15. In each case, the geometry consisted in two fibres wrapped around each other, with a given wrap angle $\gamma \in [0°, 180°]$, as detailed in Figure 15A. These geometries were generated for different values of the fibre radius and the wrap angle. In each case, the maximum value of $\bar{\alpha}^{\text{th}}$ resulting in the separation of the two fibres are reported in Figure 15C.

When $\gamma \neq 0°$, the values of $\bar{\alpha}^{\text{th}}$ appear to be almost constant for a given radius, with mean values equal to 21.7°, 17.8° and 15.2° if $\bar{r} = 2.5$ vx, 5 vx and 10 vx, respectively. As a conclusion, this separation method is very efficient on various morphologies of wavy touching fibres regardless the wrap angle.

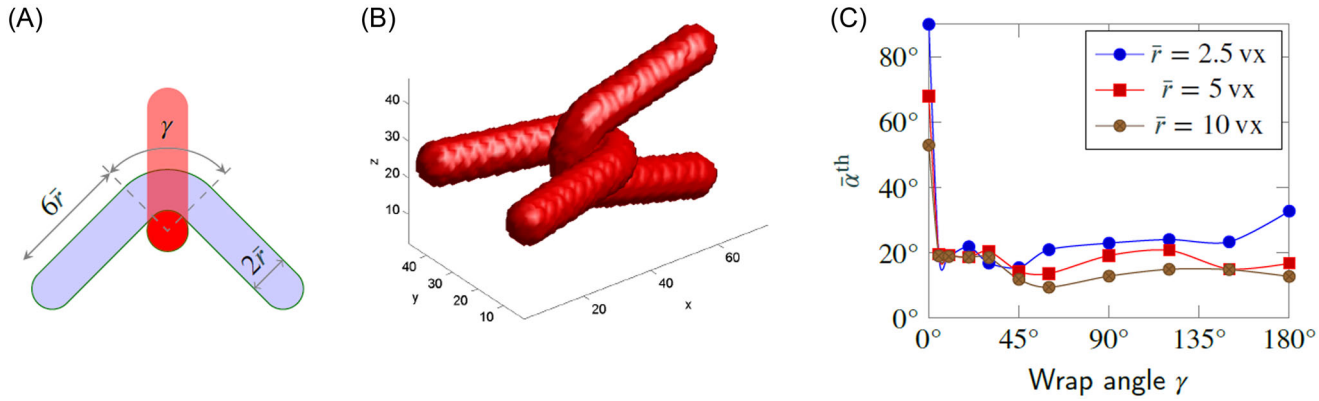

FIGURE 15 Separation of wavy touching fibres: (A) schematic view of the synthetic geometry, introducing the wrap angle and (B) example of geometry with $\gamma = 150°$ and $\bar{r} = 10$ vx; highest values of $\bar{\alpha}^{th}$ leading to the separation of the fibres wrap around each other, as functions of wrap angle mean fibre radius

3.5 | General guidelines to use the algorithm

Based on the previous results, the following guidelines can be provided to ensure the ability of the proposed approach to accurately separate and characterize the fibres:

- $n_t = 37$ investigated directions for the computations of chord lengths appears to be the best compromise between execution time and precision;
- each fibre should have a diameter larger than 5 vx and a slenderness ratio larger than 3;
- longitudinal dilation should be used for straight fibres, since it keeps their straightness and avoids unrealistic inter-penetration;
- isotropic dilation should be used for wavy fibres because it leads to almost zero orphan voxels at the end of recursive dilatations;
- wavy fibres can also be separated, as long as parts of them are straight segments.

No guideline has been raised about the choice for $\bar{\alpha}^{th}$. Since it is used as a global parameter (depending on the type of fibrous network), one can simply find the adequate value by trial-and-error.

4 | APPLICATION: FIBRE IDENTIFICATION IN VARIOUS FIBRE NETWORKS

4.1 | Considered media

In order to investigate the ability of the proposed algorithm to separate and reconstruct the fibres on complex media, CT images of various materials were used, as summed up in Figure 16. These media were chosen to investigate whether the proposed algorithm can be applied for fibre identification in various volume fraction of fibres (e.g. A vs. B), for various shapes of fibres' cross sections (e.g. A vs. C), for various fibres orientations distributions (e.g. A vs. B), for straight and woven fibres (e.g. B vs. D) and even on filament tows (E).

The fibrous medium (A) was constituted of short pieces of nylon fibres of identical length.[35] Medium (B) was constituted of short carbon fibres of different lengths embedded in a polymer matrix. Medium (C) was a sheet moulding compound (SMC) made up of planar random glass fibre bundles.[36] Medium (D) was imaged during an in situ bias test of a woven textile (plain weave of metallic fibres with circular cross sections). Medium (E) was an artificial 3D image of a woven textile, where each yarn consisted in a series of slender filaments with circular cross section. This image was generated using the WeaveGeo module as part of the Geodict software.[37] Medium (A) was imaged on TOMCAT beamline at the Swiss Light Source (SLS). Medium (B) was imaged on ID19 beamline at the European Synchrotron Radiation Facility (ESRF). Media (C) and (D) were imaged on a laboratory tomograph (3SR Lab, RX Solutions apparatus). The structural properties of each medium are detailed in Table 2. In each case, the threshold value of the misorientation angle ($\bar{\alpha}^{th}$) used for separation and the kernel used for dilations ($\mathscr{D}$) are given in this table.

4.2 | Straight short fibres

Figure 17A represents the fibres identified in the medium composed of nylon fibres (see Figure 16A). A total of 1318 distinct fibres were identified.

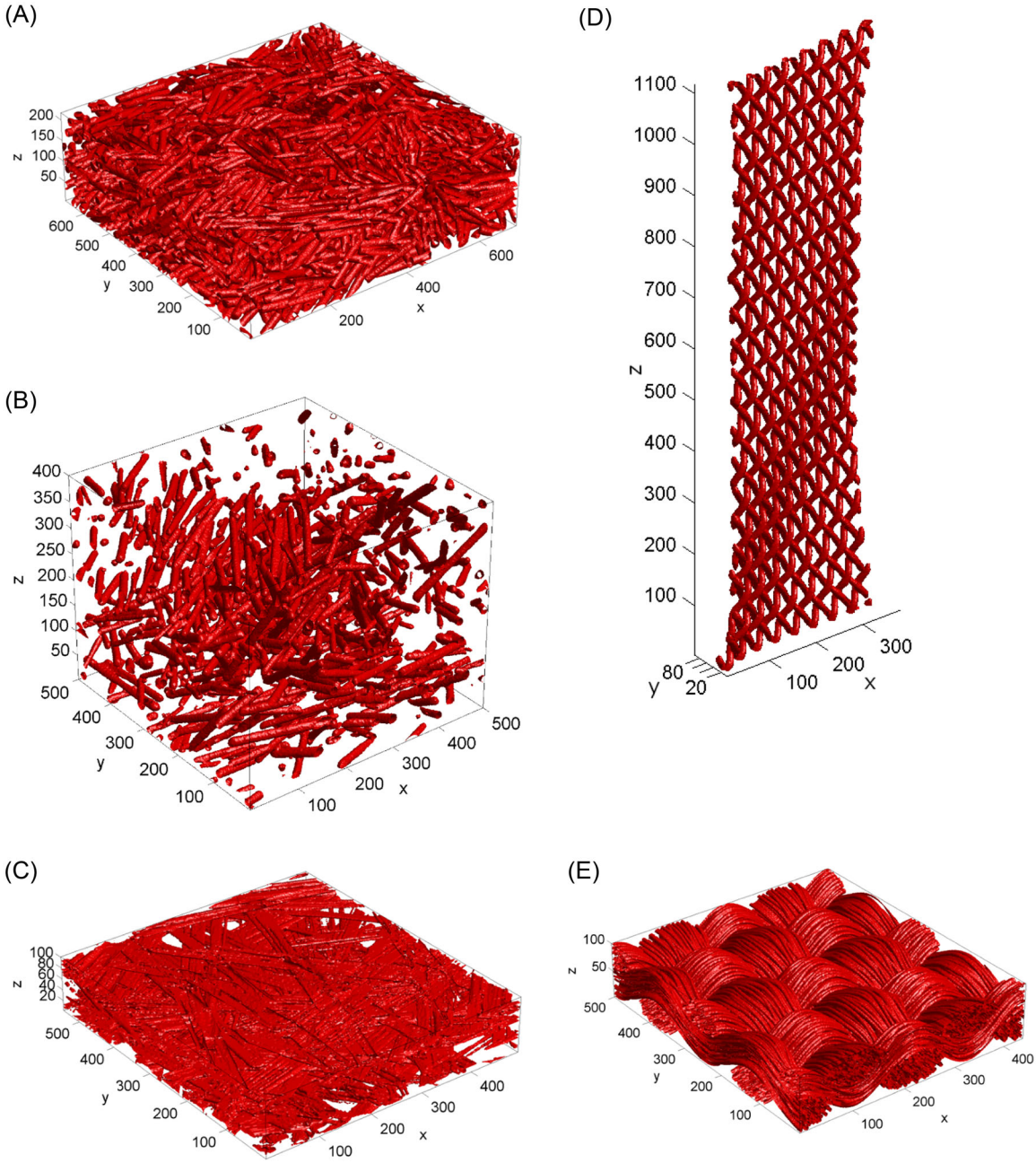

FIGURE 16 3D images of the investigated media: (A) nylon fibres in candle gel, (B) carbon fibres in polymer matrix, (C) sheet moulding compound, (D) woven textile with monofilament with circular cross section, (E) woven fabric (plain weave) with filament-based yarns (synthetic)

TABLE 2 Properties of the media used as applications of the proposed approach, presented in Figure 16, and corresponding parameters used for separation ($\tilde{\alpha}^{\mathrm{th}}$) and reconstruction ($\mathcal{D}$)

	Material	Volume fraction	Nominal diameter	$\tilde{\alpha}^{\mathrm{th}}$	$\mathcal{D}$
(A)	Nylon fibres	33.4%	16 vx	4°	Longitudinal
(B)	Carbon fibres	6.12%	11 vx	4°	Longitudinal
(C)	SMC	25.9%	–	4°	Longitudinal
(D)	Woven fibres	5.76%	10 vx	10°	Isotropic
(E)	Woven tows of fibres	43.1%	300 fib./tow, fib.: 4 vx	8°	Isotropic

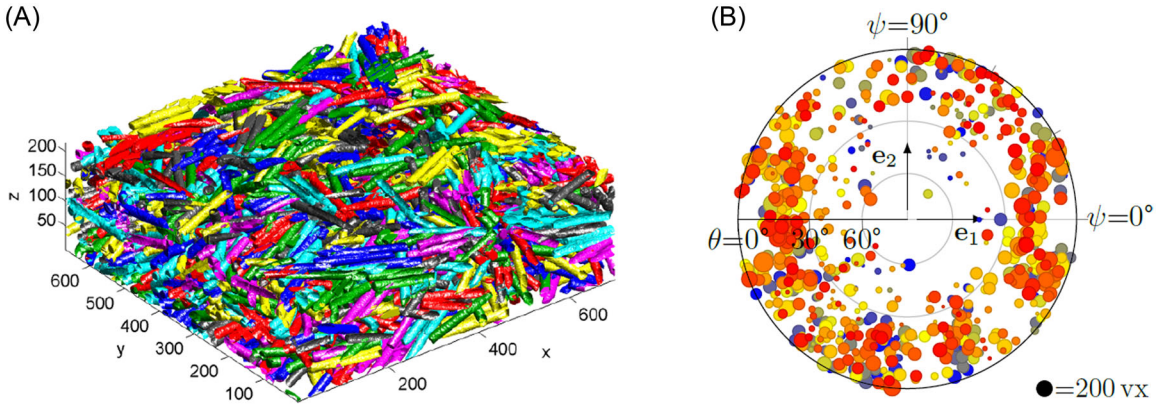

FIGURE 17 Result from separation of nylon fibres: (A) 3D representation and (B) pole figure illustrating the mean orientation of each fibre; a unique colour is attributed to each fibre; dot size is related to the corresponding fibre length

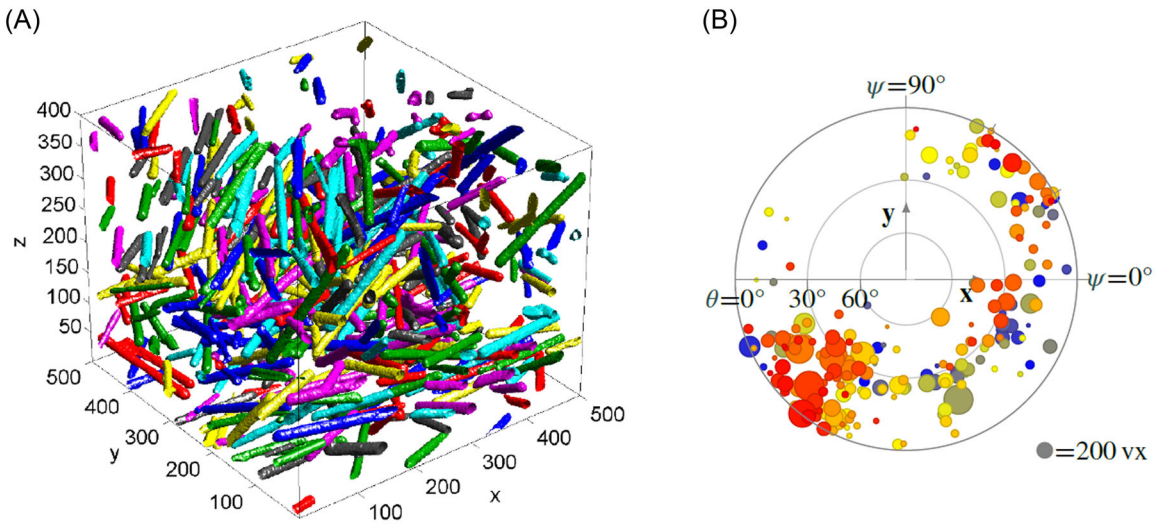

FIGURE 18 Result from separation of carbon fibres: (A) 3D representation and (B) pole figure illustrating the mean orientation of each fibre; a unique colour is attributed to each fibre; the dot size is related to the corresponding fibre length

The mean orientation of each fibre is presented in the Pole Figure 17B. In this figure, the diameter of each dot is related to the corresponding fibre length. One can see a near transverse isotropic orientation distribution, with almost all fibres nearly lying along the horizontal plane (x, y), with $\theta < 30°$. In Figure 17A, one can see that if two fibres are in contact and nearly parallel to each other, they cannot be separated. This is in accordance with the cases corresponding to the lower values of β in Section 3.3.

4.3 | Polydisperse and randomly oriented short fibres

Figure 18A represents carbon fibres (introduced in Figure 16B) after separation, where 446 fibres were identified. From this figure, it appears that the present algorithm is able to separate randomly oriented fibres (3D distribution), while that proposed by Viguié et al.[27] is only efficient if fibres show a near-planar distribution. Figure 18B represents the mean orientation of each fibre (the dot size is related to the corresponding fibre length), emphasizing that the orientation distribution is fully 3D.

4.4 | Sheet moulding compound

Figure 19 shows the identified fibres in the SMC. It appears that most of the fibres were identified despite the random shapes of their cross sections. From these data, the contacts were identified, leading to a coordination number (defined

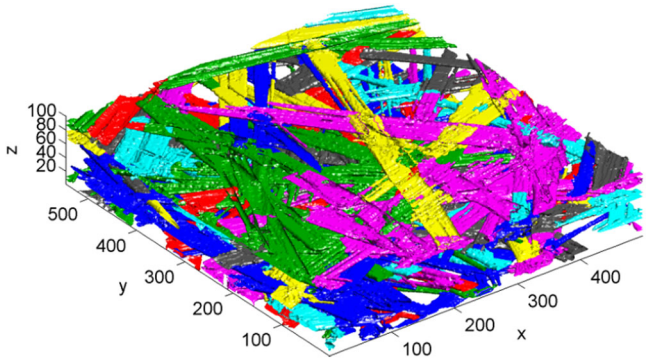

FIGURE 19 Result of separation of the fibres in an SMC. A unique colour is randomly attributed to each fibre

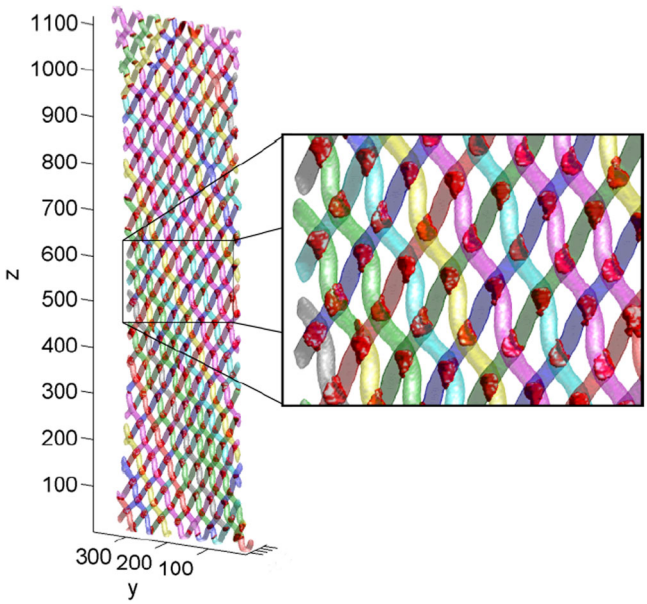

FIGURE 20 Illustration of the contact zones found in the woven fibres, shown in red (fibres are represented in transparency)

as the mean number of fibre–fibre contact per fibre) equal to 6.57. This value is similar to the ones reported in other SMCs.[38] In Figure 19, it appears that the fibres are well-separated despite their random cross sections and their highly anisotropic cross sections. Nevertheless, some fibres have been broken up by the separation, since they appear discontinuous. These splits may be due to the low number of voxels in thickness combined with a large coordination number.

4.5 | Woven plain weave of circular wires

Figure 20 illustrates the application of the present algorithm on the image from the in situ bias test (introduced in Figure 16D). Efforts were made to keep each fibre connected despite the large number of fibre–fibre contacts,

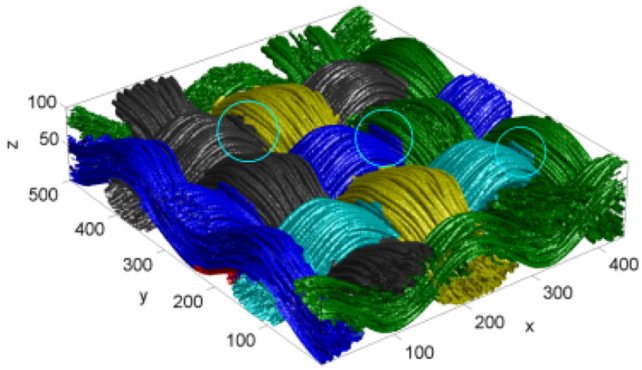

FIGURE 21 Identified fibres after separation of the textile composed of filament yarns. The circles show locations where the contacts are not accurately defined

leading to local break-up of the fibres. It appears that the contacts are well retrieved despite the moderate waviness of the wires.

4.6 | Woven plain weave of dense yarns

Attempts were made to separate the tows from the binary image of a textile constituted of filament tows (introduced in Figure 16D), as depicted in Figure 21. After separation, it appears that each yarn is well separated from each other, despite the woven structure and the large volume fraction. Nevertheless, some regions appear to be allocated to wrong fibres near contacts (see circles in Figure 21). Indeed, because of the filaments, each tow can be divided into subregions. The difficulty of separating such a medium is because it can be considered at different scales: the filament or the tow scale. In addition, because the filaments within each tow are nearly parallel, the proposed algorithm is unable to properly separate them. Thus, other techniques based on morphological analysis[5–7] or skeletonization[8,10] may be used in such a context.

4.7 | Performances

The computational time of the methods proposed in this paper are strongly dependent on the medium. For instance, the computation time of the chord lengths is linear with the number of voxel in Ω^{f}, that is, linear time with the volume fraction and the volume of the CT image. Since the Least-Misorientation method (detailed in Section 2.4.2) requires to consider each fibre at a time, it runs in linear time with n_{f}. This algorithm was developed in MATLAB®, using the Parallel Computing and Image Processing toolboxes. Hence, some routines were parallelized

(e.g. local orientations and recursive dilations) in order to speed up the process. In addition, the dilation operations (used in Sections 2.4 and 2.5.3) take advantage of bit packing,[39] making the corresponding algorithms very efficient. Among all media presented in Section 4, the image of nylon fibres (Figure 17A) lead to the longest computational time (about 36 h on a 6-core CPU). Finally, it is worth mentioning that this time could by highly reduced by using graphics processing unit (GPU) computing.

5 | GENERAL CONCLUSION

We proposed a method to identify the solid fibres in various fibrous media with volume fraction up to 45%. Starting from binary 3D images, chord lengths and inertia matrices, as introduced by Altendorf and Jeulin,[26] are computed first; then the misorientation angle is used as a criterion for separation. In order to fully reconstruct the fibres geometries, two dilation algorithms were studied (namely, isotropic and longitudinal). As a result, this approach relies on three main parameters: the threshold value on misorientation, the number of considered neighbours for the computation of the chord lengths, and the dilation operator to be used. All these parameters were analysed, leading to optimum values, depending on the properties of the fibrous network. This approach works well, even on complex media such as:

- high volume fraction of fibres,
- random cross sections,
- wavy fibres.

The efficiency of the proposed method for separating the fibres was evaluated on elementary cases. It was shown that a minimum radius of 5 vx and a slenderness ratio larger than 3 is required to ensure the fibre separation between straight fibres in contact to each other. The error made on the radii and the fibres orientations was estimated. For woven fibres, no restriction on the fibre radius was observed.

Since the fibres can be separated, the contact surface between them can be evaluated. In order to get more detailed information about the contacts, one may mesh the corresponding surface (instead of using the regular grid, inherited from the voxels), for instance using the marching cube method,[40] based on the grey level of CT images.

In this paper, the fibres are either considered as wavy or perfectly straight. In a further work, the fibres may be defined piecewise, allowing to investigate the local orientations (such as bending) and local cross sections. This improvement may be in great interest for the dilation procedure.

AUTHOR'S CONTRIBUTIONS

The contributions of the authors are the following: L.O, B.L. and S.R. conceived the study; D.D., L.O. and S.R. discussed the algorithms to be developed and the validation tests to be carried out to identify fibres and fibre–fibre contacts; D.D. developed the code; D.D. and S.R. wrote the manuscript; all the authors analysed the results and revised the manuscript before submission.

ACKNOWLEDGEMENTS

This work was supported by the Michelin Corporation, 23 place Carmes Déchaux, 63000 Clermont Ferrand, FRANCE through a research contract, as part of the PHARE project. The 3SR Lab is part of LabEx Tec 21 (ANR-11-LABX-0030) and of Institut Carnot PolyNat (ANR16-CARN-0025).

ORCID

Sabine Rolland du Roscoat https://orcid.org/0000-0003-0306-1418

References

1. Picu, C. R. (2020). Mechanics of random fiber networks: Structure–properties relation. In C. Picu & J.-F. Ganghoffer (Eds.), *Mechanics of fibrous materials and applications* (pp. 1–61). Springer International Publishing.
2. Baaklini, G. Y., Bhatt, R. T., Eckel, A. J., Engler, P., Rauser, R. W., & Castelli, M. G. (1995). X-ray microtomography of ceramic and metal matrix composites. *Materials Evaluation*, *53*(9), 1040–1044.
3. London, B., Yancey, R. N., & Smith, J. (1990). High-resolution X-ray computed tomography of composite materials. *Materials Evaluation*, *48*, 604–608.
4. Summerscales, J. (1990). *Non-destructive testing of fibre-reinforced plastics composites* (Vol. 2). Springer Science & Business Media.
5. Hessman, P. A., Riedel, T., Welschinger, F., Hornberger, K., & Böhlke, T. (2019). Microstructural analysis of short glass fiber reinforced thermoplastics based on x-ray micro-computed tomography. *Composites Science and Technology*, *183*, 107752.
6. Masse, J. P., Salvo, L., Rodney, D., Bréchet, Y., & Bouaziz, O. (2006). Influence of relative density on the architecture and mechanical behaviour of a steel metallic wool. *Scripta Materialia*, *54*(7), 1379–1383.
7. Rosini, S., Mavrogordato, M. N., Egorova, O., Matthews, E. S., Jackson, S. E., Mark Spearing, S., & Sinclair, I. (2019). In situ statistical measurement of local morphology in carbon-epoxy composites using synchrotron x-ray computed tomography. *Composites Part A: Applied Science and Manufacturing*, *125*, 105543.
8. Russ, J. C., & Woods, R. P. (1995). The image processing handbook. *Journal of Computer Assisted Tomography*, *19*(6), 979–981.
9. Wernersson, E., Borodulina, S., Kulachenko, A., & Borgefors, G. (2014). Characterisations of fibre networks in paper using micro computed tomography images. *Nordic Pulp & Paper Research Journal*, *29*(3), 468–475.

10. Latil, P., Orgéas, L., Geindreau, C., Dumont, P., & du Roscoat, S. R. (2011). Towards the 3D in situ characterisation of deformation micro-mechanisms within a compressed bundle of fibres. *Composites Science and Technology*, *71*(4), 480–488.
11. Requena, G., Fiedler, G., Seiser, B., Degischer, P., Michiel, M. D., & Buslaps, T. (2009). 3D-quantification of the distribution of continuous fibres in unidirectionally reinforced composites. *Composites Part A: Applied Science and Manufacturing*, *40*(2), 152–163.
12. Bonnassie, A., Peyrin, F., & Attali, D. (2003). A new method for analyzing local shape in three-dimensional images based on medial axis transformation. *IEEE Transactions on Systems, Man, and Cybernetics, Part B: Cybernetics*, *33*(4), 700–705.
13. Orgéas, L., Dumont, P. J. J., Vassal, J.-P., Guiraud, O., Michaud, V., & Favier, D. (2012). In-plane conduction of polymer composite plates reinforced with architectured networks of copper fibres. *Journal of Materials Science*, *47*(6), 2932–2942.
14. Lux, J., Delisée, C., & Thibault, X. (2011). 3D characterization of wood based fibrous materials: An application. *Image Analysis & Stereology*, *25*(1), 25–35.
15. Tan, J. C., Elliott, J., & Clyne, T. W. (2006). Analysis of tomography images of bonded fibre networks to measure distributions of fibre segment length and fibre orientation. *Advanced Engineering Materials*, *8*(6), 495–500.
16. Yang, H., & Lindquist, W. B. (2000). Three-dimensional image analysis of fibrous materials. In *International Symposium on Optical Science and Technology* (pp. 275–282). International Society for Optics and Photonics.
17. Malmberg, F., Lindblad, J., Östlund, C., Almgren, K. M., & Gamstedt, E. K. (2011). Measurement of fibre–fibre contact in three-dimensional images of fibrous materials obtained from x-ray synchrotron microtomography. *Nuclear Instruments and Methods in Physics Research Section A: Accelerators, Spectrometers, Detectors and Associated Equipment*, *637*(1), 143–148.
18. Svensson, S., & Aronsson, M. (2003). Using distance transform based algorithms for extracting measures of the fiber network in volume images of paper. *IEEE Transactions on Systems, Man, and Cybernetics, Part B (Cybernetics)*, *33*(4), 562–571.
19. Krause, M., Hausherr, J. M., Burgeth, B., Herrmann, C., & Krenkel, W. (2009). Determination of the fibre orientation in composites using the structure tensor and local x-ray transform. *Journal of Materials Science*, *45*(4), 888–896.
20. Naouar, N., Vidal-Sallé, E., Schneider, J., Maire, E., & Boisse, P. (2014). Meso-scale FE analyses of textile composite reinforcement deformation based on x-ray computed tomography. *Composite Structures*, *116*, 165–176.
21. Eberhardt, C. N., & Clarke, A. R. (2002). Automated reconstruction of curvilinear fibres from 3D datasets acquired by x-ray microtomography. *Journal of Microscopy*, *206*(1), 41–53.
22. Naouar, N., Vidal-Salle, E., Schneider, J., Maire, E., & Boisse, P. (2015). 3D composite reinforcement meso F.E. analyses based on x-ray computed tomography. *Composite Structures*, *132*, 1094–1104.
23. Haralick, R. M., & Shapiro, L. G. (1985). Image segmentation techniques. *Computer Vision, Graphics, and Image Processing*, *29*(1), 100–132.
24. Miletić, M., Kumar, L. M., Arns, J.-Y., Agarwal, A., Foster, S. J., Arns, C., & Perić, D. (2020). Gradient-based fibre detection method on 3D micro-CT tomographic image for defining fibre orientation bias in ultra-high-performance concrete. *Cement and Concrete Research*, *129*, 105962.
25. Sandau, K., & Ohser, J. (2007). The chord length transform and the segmentation of crossing fibres. *Journal of Microscopy*, *226*(1), 43–53.
26. Altendorf, H., & Jeulin, D. (2009). 3d directional mathematical morphology for analysis of fiber orientations. *Image Analysis & Stereology*, *28*(3), 143–153.
27. Viguié, J., Latil, P., Orgéas, L., Dumont, P., du Roscoat, S. R., Bloch, J.-F., Marulier, C., & Guiraud, O. (2013). Finding fibres and their contacts within 3D images of disordered fibrous media. *Composites Science and Technology*, *89*, 202–210.
28. Miettinen, A., Ojala, A., Wikström, L., Joffe, R., Madsen, B., Nättinen, K., & Kataja, M. (2015). Non-destructive automatic determination of aspect ratio and cross-sectional properties of fibres. *Composites Part A: Applied Science and Manufacturing*, *77*, 188–194.
29. Haralick, R. M., Shanmugam, K., & Dinstein, I. (1973). Textural features for image classification. *IEEE Transactions on Systems, Man, and Cybernetics*, *SMC-3*(6), 610–621.
30. Hong, L., Zhang, P., Liu, D., Gao, P., Zhan, B., Yu, Q., & Sun, L. (2021). Effective segmentation of short fibers in glass fiber reinforced concrete's x-ray images using deep learning technology. *Materials & Design*, *210*, 110024.
31. Yosifov, M. I. (2020). *Extraction and quantification of features in XCT datasets of fibre reinforced polymers using machine learning techniques* (Master's thesis). Umeå University, Department of Computing Science.
32. Soille, P. (2013). *Morphological image analysis: Principles and applications*. Springer Science & Business Media.
33. Haralick, R. M., Sternberg, S. R., & Zhuang, X. (1987). Image analysis using mathematical morphology. *IEEE Transactions on Pattern Analysis and Machine Intelligence*, (4), 532–550.
34. Woodcock, N., & Naylor, M. (1983). Randomness testing in three-dimensional orientation data. *Journal of Structural Geology*, *5*(5), 539–548.
35. Laurencin, T., Orgéas, L., Dumont, P., du Roscoat, S. R., Laure, P., Corre, S. L., Silva, L., Mokso, R., & Terrien, M. (2016). 3D real-time and in situ characterisation of fibre kinematics in dilute non-newtonian fibre suspensions during confined and lubricated compression flow. *Composites Science and Technology*, *134*, 258–266.
36. Ferré Sentis, D., Orgéas, L., Dumont, P., Rolland du Roscoat, S., Sager, M., & Latil, P. (2017). 3D in situ observations of the compressibility and pore transport in sheet moulding compounds during the early stages of compression moulding. *Composites Part A: Applied Science and Manufacturing*, *92*, 51–61.
37. Wiegmann, A., Becker, J., Cheng, L., Glatt, E., & Rief, S. (2011). Geodict: A software-centered approach to the simulation of thin porous media and their properties. In *Proceedings of 3rd International Conference on Porous Media*, Bordeaux, France.
38. Meyer, N., Schöttl, L., Bretz, L., Hrymak, A., & Kärger, L. (2020). Direct bundle simulation approach for the compression molding process of sheet molding compound. *Composites Part A: Applied Science and Manufacturing*, *132*, 105809.
39. van den Boomgaard, R., & van Balen, R. (1992). Methods for fast morphological image transforms using bitmapped binary images. *CVGIP: Graphical Models and Image Processing*, *54*(3), 252–258.

40. Lorensen, W. E., & Cline, H. E. (1987). Marching cubes: A high resolution 3D surface construction algorithm. In *ACM SIGGRAPH Computer Graphics* (pp. 163–169). ACM.

How to cite this article: Depriester, D., et al. (2022). Individual fibre separation in 3D fibrous materials imaged by X-ray tomography. *Journal of Microscopy*, 1–20. https://doi.org/10.1111/jmi.13096

APPENDIX A: COMPUTATION OF THE CHORD LENGTHS

In this paper, the method proposed by Altendorf and Jeulin[26] have been used to compute the chord lengths at voxel P, denoted d_P here. Figure A1 schematically illustrates how $d_j(\mathbf{t}^i)$ and $d_j(-\mathbf{t}^i)$ are defined.

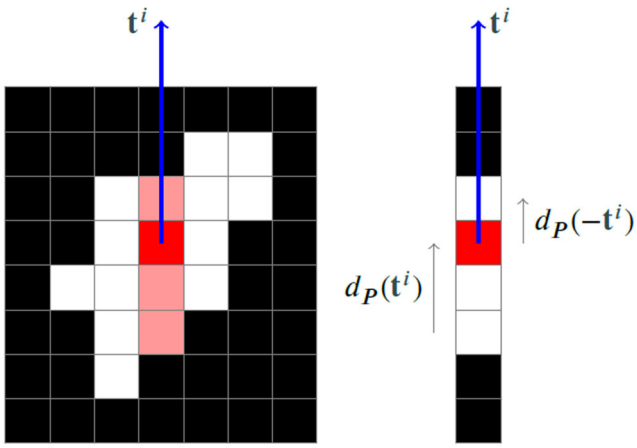

FIGURE A1 Schematic representation of the method used for computing of the chord lengths d_j along a given direction $\mathbf{t}^i$ at a given location (red square): the white squares illustrate the fibrous phase nested in the matrix (black squares)

APPENDIX B: INVESTIGATED DIRECTIONS FOR COMPUTATION OF THE CHORD LENGTHS

According to the definition of the half-chord length $\mathrm{d}c_P(\mathrm{t}^i)$, given in (1), it is clear that $\mathrm{d}c_P(-\mathbf{t}^i) = \mathrm{d}c_P(\mathrm{t}^i)$. This means that the computation of $\mathbf{I}_P$ based on the N-connected neighbourhood can be reduced to $n_t = N/2$ directions. In addition, because of the way the chord lengths are computed $\mathrm{d}c_P(\mathrm{t}^i)$ (see for instance Figure A1), it appears that:

$$\forall k, \quad \mathrm{d}c_P\left(k\mathbf{t}^i\right) = \mathrm{d}c_P(\mathrm{t}^i). \tag{B1}$$

In other words, if $\mathrm{d}c_P(\mathrm{t}^i)$ has already been computed, the computation of the half-chord length along any direction parallel to $\mathbf{t}^i$ would be redundant for the evaluation of $\mathbf{I}_P$. Thus, all sets of computational directions $\mathbf{t}^i$ used for computing the chord lengths, as investigated in Section 3.1, are presented in Figure B1.

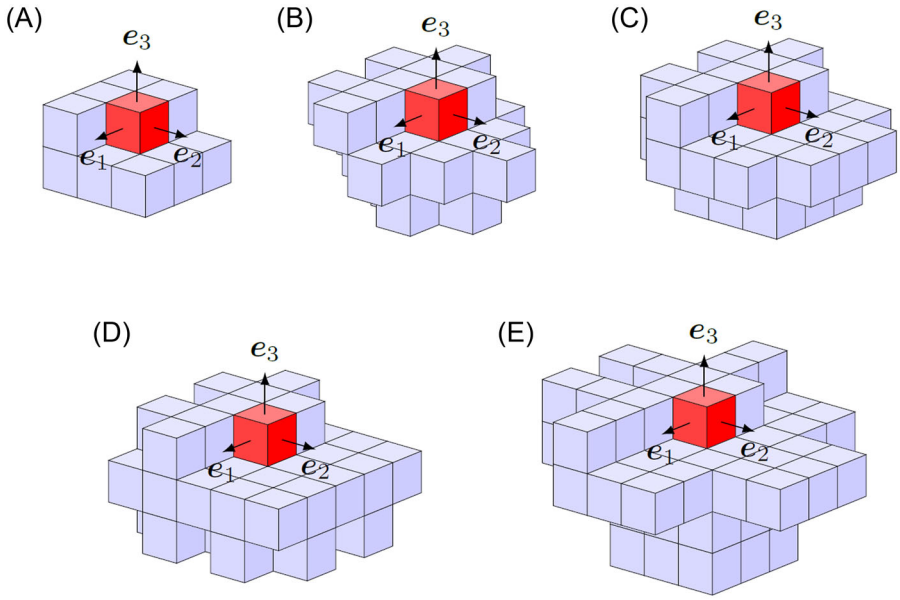

FIGURE B1 Illustration of the investigated computational directions of the chord lengths from a given voxel: the reference voxel (where the chord lengths are computed) is represented in red and its considered neighbours are represented in blue. (A) $n_t = 13$, (B) $n_t = 25$, (C) $n_t = 37$, (D) $n_t = 49$ and (E) $n_t = 61$